Advanced Energy Materials

ADVANCED ENERGY MATERIALS
www.advenergymat.de

RESEARCH ARTICLE OPEN ACCESS

Cold-Sublimating Quasi-Solid Additive Enables High Efficiency and Long Operational Stability Binary Organic Solar Cells

Zesheng Zhang[1,2] | Lingchen Kong[1,5] | Xinkang Wang[1] | Rong Wang[2,3] | Hua Tang[2] | Mingqing Chen[1] | Yuntong Yang[1] | Lianjie Zhang[1] | Yuang Fu[6] | Xinhui Lu[6] | Dongge Ma[1] | Larry Lüer[2] | Chao Liu[2,3] | Christoph J. Brabec[2,3,4] | Junwu Chen[1]

[1]Institute of Polymer Optoelectronic Materials & Devices, Guangdong Basic Research Center of Excellence for Energy & Information Polymer Materials, State Key Laboratory of Luminescent Materials & Devices, South China University of Technology, Guangzhou, P. R. China | [2]Institute of Materials for Electronics and Energy Technology (i-MEET), Friedrich-Alexander-Universität Erlangen-Nürnberg (FAU), Erlangen, Germany | [3]Helmholtz-Institute Erlangen-Nürnberg (HI ERN), Erlangen, Germany | [4]Institute of Energy Materials and Devices (IMD-3), Forschungszentrum Jülich GmbH Wilhelm-Johnen-Straße, Jülich, Germany | [5]Department of Material Science & Engineering, City University of Hong Kong, Kowloon, Hong Kong, China | [6]Department of Physics, The Chinese University of Hong Kong, New Territories, Hong Kong 999077, P. R. China

Correspondence: Chao Liu (c.liu@fz-juelich.de) | Christoph J. Brabec (christoph.brabec@fau.de) | Junwu Chen (psjwchen@scut.edu.cn)

Received: 18 September 2025 | **Revised:** 15 November 2025 | **Accepted:** 20 November 2025

Keywords: additive engineering | cold sublimation | in situ removable solid additive | organic solar cell | thermal stability

ABSTRACT

Controlling activelayer morphology during drying is pivotal for the simultaneous realization of high efficiency and durability in Yseries organic solar cells (OSCs). Here, we uncover how the physical state of in situ removable (ISR) isomeric additives, *o*DF (liquid), *m*DF (quasisolid), and *p*DF (solid), governs film formation, molecular ordering, and device stability in binary OSCs. Among them, quasisolid *m*DF functions as a coldsublimating transient structuring agent: it widens earlystage solvent removal window yet accelerates intermediate crystallization, tightens π–π stacking, enlarges coherence length, and programs a favorable vertical phase separation, as resolved by in situ UV–vis, GIWAXS, and depthprofiled spectroscopy. *m*DF interacts most strongly with L8-BO while fully evaporating from the film, minimizing nonradiative losses and avoiding the adverse impact of residual additives on device stability. Consequently, PM6:L8BO devices reach 19.28% PCE with improved carrier mobility and suppressed trapassisted recombination; applying *m*DF to D18:L8BO yields 20.08%. Under 1sun illumination at 70 °C, *m*DF extends operational stability to T_{80} = 477 h, outperforming *o*DF (58 h), *p*DF (279 h), and additivefree control (103 h). These results establish physicalstateprogrammed ISR additives as a general route to cooptimize efficiency and stability in OSCs and provide mechanistic guidance for scalable, residuefree morphology control.

1 | Introduction

Organic solar cells (OSCs) integrate solution processability, lightweight, semi-transparency, and mechanical flexibility, positioning them as a transformative technology for portable devices, building-integrated photovoltaics, and wearable electronics [1–5]. Over the past decades, continuous advancements in active layer materials, particularly the emergence of transformative Y-series non-fullerene acceptors (NFAs), have propelled the power conversion efficiency (PCE) of bulk-heterojunction (BHJ) OSCs beyond the 20% benchmark in both single-junction and tandem architectures [6–12]. These groundbreaking achievements

firmly establish OSCs as a promising candidate for commercialization, contingent upon overcoming challenges related to long-term operational stability and scalable fabrication [13–16]. High-efficiency BHJ OSCs fundamentally rely on an optimized interpenetrating donor-acceptor network that should simultaneously maximize donor/acceptor interfacial area for efficient exciton dissociation while preserving continuous pathways for efficient charge transport [17]. An optimal BHJ morphology, characterized by well-controlled domain sizes, high crystallinity, and uniform vertical phase distribution, is pivotal for achieving exceptional device performance and ensuring long-term device stability [18–21]. Various strategies have been devised to optimize BHJ morphology, including thermal annealing, solvent vapor annealing, and additive-assisted techniques [22–25]. Among these, additive engineering has recently emerged as the most prominent focus of research, recognized for its versatility and exceptional effectiveness [26].

Additive engineering plays a crucial role in tailoring the morphology of BHJ layers by modulating the phase separation dynamics and influencing the crystallization behavior of donor and acceptor materials during spin-coating and/or post-processing of the film [27–31]. Liquid additives (LAs), typically high boiling point (bp.) solvents such as 1,8-diiodooctane (DIO) [32] and 1-chloronaphthalene (CN) [33], have been extensively utilized to regulate the drying kinetics of the BHJ solution. By decelerating/regulating solvent evaporation, LAs facilitate the formation of refined BHJ morphology, characterized by enhanced molecular packing and greater domain purity, ultimately boosting device performance [34]. However, these high b.p LAs require additional vacuum extraction steps to be eliminated from the active layers, which increases fabrication complexity and cost for large-scale manufacturing. Moreover, these LA residuals can induce photo-oxidative degradation of active layers under light stress, compromising long-term device reliability [35]. In response to these limitations, solid additives (SAs) have emerged as a promising alternative [36, 37]. Representative small organic molecules, such as diiodobenzene (DIB) [38–40], dithieno[3,2-b:2′,3′-d]thiophene (DTT) [41], and 2-chloronaphthalene (2-CN) [42], exhibit distinct advantages over LAs [43–45]. Unlike their liquid counterparts, SAs can selectively interact with donor or acceptor materials via noncovalent interactions, enabling precise modulation of vertical component distribution and improved film quality [46–49]. SAs can be categorized into volatile and non-volatile types: volatile SAs can be removed completely out of the active layer during processing, while non-volatile SAs remain embedded in the film, causing the deterioration of long-term performance [50]. Notably, volatile SAs have gained significant attention due to their simple molecular structures, wide commercial availability, and compatibility with large-scale fabrication processes [51]. However, most SAs are removed via high-temperature annealing (hot sublimation) to enable optimal morphology [52, 53]. In situ removable (ISR) SAs address these limitations by coldsublimating with the host solvent during film drying, enabling residuefree morphology programming without vacuum extraction or hot sublimation [10, 11]. Thus, no mass transfer occurred during the subsequent thermal annealing process, which can provide higher safety by preventing the spread of SA in the environment and its inhalation by human beings. Despite this promise, the role of the additive's physical state (liquid, quasisolid, solid) in dictating drying kinetics, crystallization pathways, and longterm device stability remains insufficiently resolved.

In this work, we introduce a physicalstateprogrammed ISR strategy in PM6:L8BO based OSCs by utilizing three isomeric dibromodifluorobenzene additives, *o*DF (liquid), *m*DF (quasisolid), and *p*DF (solid), to explore the influence of additives' physical states and thermal properties on the evaporation dynamics and molecular interactions during film formation, thereby determining the morphology of the active layer and the overall device performance. Through a complementary characterization combination of UV–vis absorption spectroscopy, X-ray diffraction, and computational simulations, we clearly reveal the distinct effect of these additives on the molecular packing, charge transport, and film structure. Notably, quasi-solid *m*DF emerges as a transient structuring agent that widens the early solventremoval window yet accelerates intermediate crystallization, yielding tighter π–π stacking, larger coherence length, and an optimized vertical donor/acceptor distribution. Mechanistically, mDF exhibits the strongest noncovalent interaction with L8BO while fully evaporating from the film, thereby minimizing nonradiative losses. As a result, PM6:L8-BO-based binary OSCs with *m*DF exhibit a PCE of 19.28%, outperforming the control devices (17.72%), the *o*DF-(17.28%), and *p*DF-processed devices (18.54%). Remarkably, when applied to the D18:L8-BO system, *m*DF enables the binary devices to surpass a PCE of 20%, highlighting its exceptional potential for highly efficient devices. Additionally, *m*DF-treated devices exhibit superior operational stability, maintaining a T_{80} value of 477 h (80% of the initial PCE) under equivalent 1 sun illumination & 70°C, significantly outperforming those with *o*DF (T_{80} = 58 h), *p*DF (T_{80} = 279 h), and without any additive (T_{80} = 103 h). These results establish physicalstateprogrammed ISR additives as a residuefree route to cooptimize efficiency and durability in OSCs.

2 | Results and Discussion

Figure 1a presents the chemical structures of the *o*DF, *m*DF, and *p*DF together with PM6 and L8-BO. The additives span distinct physical states and thermal properties: *o*DF is a liquid (bp. 212°C), *m*DF is a quasi-solid (melting point, mp. 33°C; bp. 203.1°C), and *p*DF is a solid (mp. 62°C; bp. 209.2°C). The differences in phase and thermal behavior significantly influence the film formation dynamics and molecular packing in active layers. In addition, thermal gravimetric analysis (TGA) was performed to investigate the evaporation behavior of *m*DF and *p*DF. As illustrated in Figure S1, the thermal decomposition profiles reveal early volatilization onsets (5% weight loss) at ~65 °C for *m*DF and ~72 °C for *p*DF, with complete volatilization by ~128 °C (*m*DF) and ~109 °C (*p*DF), consistent with facile cold sublimation during drying. UV–vis absorption spectra provide an effective method to characterize the aggregation evolution of PM6 and L8-BO films. As shown in Figure S2, PM6 films exhibit only marginal enhancement in their 0–0 peaks upon additive treatment. In striking contrast, the three additives induce significantly more substantial redshifts in L8-BO films, with the *m*DF-treated film showing the most pronounced shift, as depicted in Figure 1b. This sample also shows a suppression of the amorphous peak around 1.75 eV and the second-lowest allowed electronic transition near 2.0 eV.

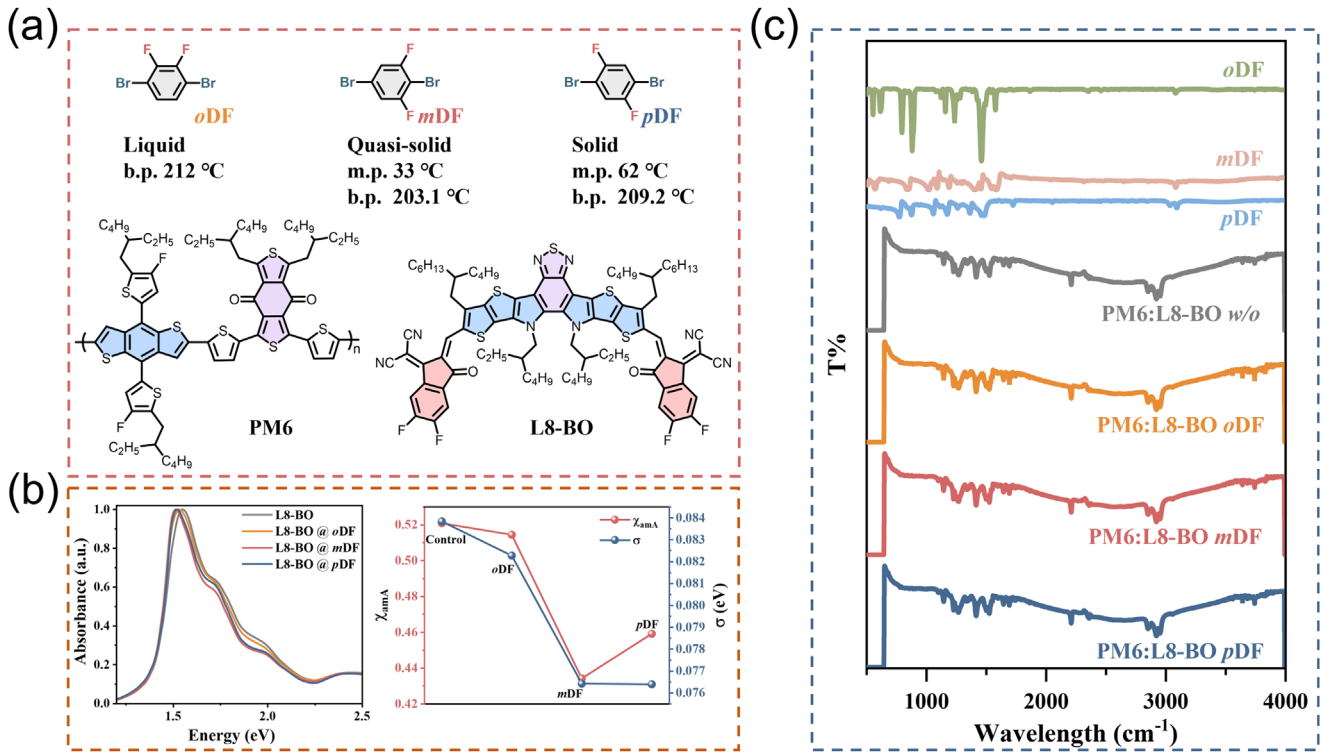

FIGURE 1 | (a) Chemical structures of *o*DF, *m*DF, *p*DF, PM6, and L8-BO. (b) UV–vis absorption spectra (left); the variation of amorphous ratio (χ_{amA}) and linewidth (σ) of the ordered A_1 peak (right) of L8-BO films without or with additives. (c) FTIR spectra of three pure additives and PM6:L8-BO blend films treated with different additives.

To elucidate the morphological evolution of L8-BO with different additives, we further analyzed the absorption spectra using a numerical model that assumes the spectra are composed of a superposition of contributions from amorphous regions (A_1, am), ordered aggregates (A_1, 0–0 transition), and the higher-energy second-lowest allowed electronic transition (A_2). Details of the fitting procedure are described in Figure S3 and references [54–59]. Each vibronic peak was modeled as a Gaussian function defined by its linewidth (σ) and center energy. The fitting results reveal a significant reduction in the amorphous fraction χ_{amA} of L8-BO upon the addition of the quasi-solid additive *m*DF, decreasing from 0.52 in pristine L8-BO to 0.43. A similar reduction in χ_{amA} is observed for the film processed with pDF; however, the broader energy distribution of the A_1 component indicates stronger exciton coupling. In contrast, the linewidth of the ordered A_1 peak narrows from 84 meV in pristine L8-BO to 76 meV with *m*DF, indicating improved molecular ordering, whereas *o*DF, as a high bp. liquid additive, but it exerts a relatively minor influence on film morphology. These findings confirm that the incorporation of quasi-solid additive, *m*DF, promotes more ordered molecular packing and reduces exciton binding energy.

To gain an in-depth understanding of the intermolecular interactions between L8-BO and various additives at the molecular level, we performed density functional theory (DFT) at the B3LYP-D3BJ/6-31G(d) level with the Gaussian 16 software package. For computational simplicity, alkyl chains were substituted with methyl groups. The "interaction region indicator" (IRI) analysis in Figure S4 reveals specific intermolecular interactions between additives and L8-BO, including steric repulsion, van der Waals forces, and hydrogen bonding. DFT calculations reveal distinct binding energies (E_b) between L8-BO and the additives: −15.42 kcal mol^{-1} (*o*DF), −16.87 kcal mol^{-1} (*m*DF), and −16.41 kcal mol^{-1} (*p*DF), respectively. Notably, quasi-solid *m*DF exhibits the strongest interaction with L8-BO, as evidenced by its most negative E_b. These significantly enhanced intermolecular forces between *m*DF and L8-BO suggest the exceptional capability to tailor the vertical morphology of the active layer in OSCs. Meanwhile, the evaporation behavior of the three additives from the active layer was further investigated using Fourier-transform infrared (FTIR) spectroscopy (Figure 1c). All tested blend films were freshly prepared without any post-treatment. All additives exhibit a characteristic transmission peak around 3085 cm^{-1}, which is absent in the as-cast PM6:L8-BO active layer. Similarly, no detectable characteristic peaks of *o*DF, *m*DF, and *p*DF are observed in PM6:L8-BO films treated with either additive, suggesting the three compounds belong to the ISR additives.

The 2D grazing-incidence wide-angle X-ray scattering (GIWAXS) patterns of neat PM6 and L8-BO films processed with or without additives are shown in Figure S5, with the corresponding 1D cut-line profiles presented in Figure S6 and detailed data summarized in Table S1. The as-cast PM6 film exhibits a predominantly face-on orientation, characterized by a (100) lamellar diffraction peak at 0.28 Å^{-1} in the in-plane (IP) direction and a (010) π–π stacking peak at 1.68 Å^{-1} in the out-of-plane (OOP) direction. Additive-treated PM6 films retain this structural motif but exhibit slightly reduced d-spacing and π–π stacking distances (denser packing), as inferred from shifts in the (100) and (010) peaks. Notably, the *m*DF-treated PM6 film demonstrates a refined molecular structure, evidenced by the largest coherence length (CL) in the

(010) π–π stacking peak. In contrast, the L8-BO films exhibit more substantial additive-induced structural modifications with the incorporation of additives. Although all three additives produce identical shifts in the (100) diffraction peak from 0.42 to 0.45 Å^{-1} in the IP direction, all contributing to tighter molecular packing, *m*DF- and *p*DF-treated films display significantly larger CLs (*m*DF: 73.05 Å; *p*DF: 83.49 Å) than *o*DF-treated films (53.13 Å), reflecting the distinct influence of additive states on molecular interactions. In the OOP direction, the quasi-solid *m*DF-treated L8-BO film features a well-defined (010) peak at 1.80 Å^{-1}, while the other two additive-treated films show an identical peak at 1.75 Å^{-1}. Additionally, the *m*DF-treated film achieves the largest CL among all samples, underscoring its superior structural refinement. All L8-BO films also exhibit (021) lamellar peaks, though their intensity varies with additive type. Compared to the as-cast film, the *o*DF-treated film shows a weaker (021) signal, whereas *m*DF- and *p*DF-treated films exhibit intensified lamellar features. Collectively, these results highlight that additive processing enhances molecular packing and CL, with *m*DF treatment yielding the most significant improvements among the additives.

In situ UV–vis absorption spectroscopy was employed to investigate the film drying mechanism. Figure 2a presents 2D contour maps of the absorption spectra recorded during spin-coating. To elucidate the impact of additives on film formation, we tracked the temporal evolution of characteristic absorption peaks for PM6 (580 and 620 nm) and L8-BO (715 and 800 nm) (Figure 2b). The results reveal four distinct stages occurring within 2 s. The first three stages (gray, blue, pink) correspond to sequential solvent removal, while the final stage (green) marks stabilization. In the gray phase, a rapid intensity drop indicates chloroform (CF) evaporation as the system transitions from liquid to solid. The blue phase, characterized by a slower decline, reflects film thinning due to centrifugation. The pink phase is mainly dominated by L8-BO aggregation. Additive incorporation significantly slows film formation, promoting the development of high-crystallinity pure domains and enhancing charge transport. All additives prolong solvent evaporation and film thinning stages while shortening the aggregation time, with the effect being most pronounced for the quasi-solid *m*DF and solid *p*DF. In contrast, the liquid additive *o*DF extends the aggregation time, as evidenced by a slight increase in peak intensity at 800 nm during the final stage, likely due to delayed *o*DF evaporation. Figure 2c further illustrates time-dependent shifts in the L8-BO peak position, revealing distinct additive-mediated crystallization kinetics. Without additives, the peak shifts steadily and stabilizes early. In contrast, additives prolong the early stage (blue), allowing greater peak shifts and enhancing molecular ordering. Notably, *m*DF and *p*DF accelerate the intermediate stage (pink), whereas *o*DF extends it. Among them, *m*DF facilitates the fastest and most efficient film stabilization, as evidenced by a sharp peak shift during the intermediate stage and rapid stabilization in the final stage.

Next, conventional OSCs with a configuration of indium tin oxide (ITO)/PEDOT:PSS/active layer/PDINN/Ag architecture were fabricated to assess the impact of additives on photovoltaic performance. PEDOT:PSS serves as a hole transport layer (HTL), while PDINN functions as a small-molecule electron transport layer (ETL). Figure 3a presents the current-voltage (*J*–*V*) curves of OSCs measured under simulated AM 1.5G irradiation (100 mW cm^{-2}), with the corresponding photovoltaic parameters summarized in Table 1. The control device (without additives) achieves a PCE of 17.72% with an open-circuit voltage (V_{OC}) of 0.889 V, short-circuit current density (J_{SC}) of 25.63 mA cm^{-2}, and a fill factor (FF) of 77.81%. The incorporation of quasi-solid *m*DF and solid *p*DF enhances both J_{SC} and FF, albeit with a slight reduction in V_{OC}, while the *p*DF-treated device achieves an improved PCE of 18.54%, with corresponding values of 0.883 V, 26.91 mA cm^{-2}, and 78.04%. Notably, the *m*DF-treated device attains a superior PCE of 19.28%, featuring a V_{OC} of 0.885 V, a J_{SC} of 27.01 mA cm^{-2}, and an FF of 80.66%. In contrast, *o*DF treatment results in an inferior PCE of 17.28%, attributed to a reduced V_{OC} of 0.867 V, J_{SC} of 25.51 mA cm^{-2}, and an FF of 78.37%. Figure 3b displays the external quantum efficiency (EQE) spectra of the corresponding devices, revealing a broad and robust photon response across 400–900 nm. The redshifted EQE profiles observed in *m*DF- and *p*DF-treated devices correlate well with their absorption spectra, contributing to enhanced J_{SC}. Integrating the EQE spectra yields J_{SC} values of 24.30, 24.27, 25.57, and 25.46 mA cm^{-2} for the as-cast, *o*DF-, *m*DF-, and *p*DF-treated devices, respectively, closely matching those derived from *J*–*V* measurements, indicating excellent consistency.

To gain further insight into charge transport properties, photoinduced charge-carrier extraction by linearly increasing voltage (photo-CELIV) was employed to evaluate the mobilities of charge carriers (Figure 3c). The calculated mobilities are 2.13×10^{-4}, 2.02×10^{-4}, 3.05×10^{-4}, and 2.63×10^{-4} cm^2 V^{-1} s^{-1} for the as-cast, *o*DF-, *m*DF-, and *p*DF-treated devices, respectively, indicating that *m*DF treatment facilitates more efficient charge transport. Furthermore, charge recombination dynamics were evaluated by analyzing the dependencies of J_{sc} and V_{oc} on light intensity (I), using the expressions $V_{oc} \propto nKTq^{-1}\ln(P_{light})$ and $J_{sc} \propto P_{light}^{S}$, respectively [57]. As shown in Figure S7a, the nearly identical slope values for all devices suggest the additives exert a negligible influence on charge dissociation. However, devices show distinct extracted n values, being 1.16, 1.23, 1.03, and 1.07 kT/q for the as-cast, *o*DF-, *m*DF-, and *p*DF-treated devices, respectively. Notably, the lowest n value achieved with *m*DF demonstrates its superior ability to suppress trap-assisted recombination (Figure S7b). A comprehensive recombination analysis was conducted by examining charge carrier lifetime and density. Figure 3d illustrates transient photovoltage (TPV) measurements, while Figure 3e displays charge extraction (CE) results. The recombination exponent (λ) was determined utilizing the equation $\tau = \tau_0(n_0/n)^{\lambda}$, where τ and n represent charge carrier lifetime and density, respectively, and τ_0 and n_0 are constants. The recombination order (R) is given by $R = \lambda + 1$, where $R = 2$ denotes ideal bimolecular recombination, and higher values suggest trap-assisted recombination. The R values, derived from integrated TPV and CE measurements (Figure 3f), are 2.32, 2.19, 2.03, and 2.07 for the as-cast, *o*DF-, *m*DF-, and *p*DF-treated devices, respectively, indicating that the *m*DF-treated device yields the lowest trap density. These findings are consistent with light-intensity-dependent measurements.

Compared to the additive-free device, it is noted that those treated with the three additives exhibit notable differences in V_{OC}. As commonly observed with high bp. Additives (e.g., DIO, CN), the *o*DF-treated device shows a significantly lower V_{OC}, whereas the *m*DF- and *p*DF-treated devices maintain values comparable to the

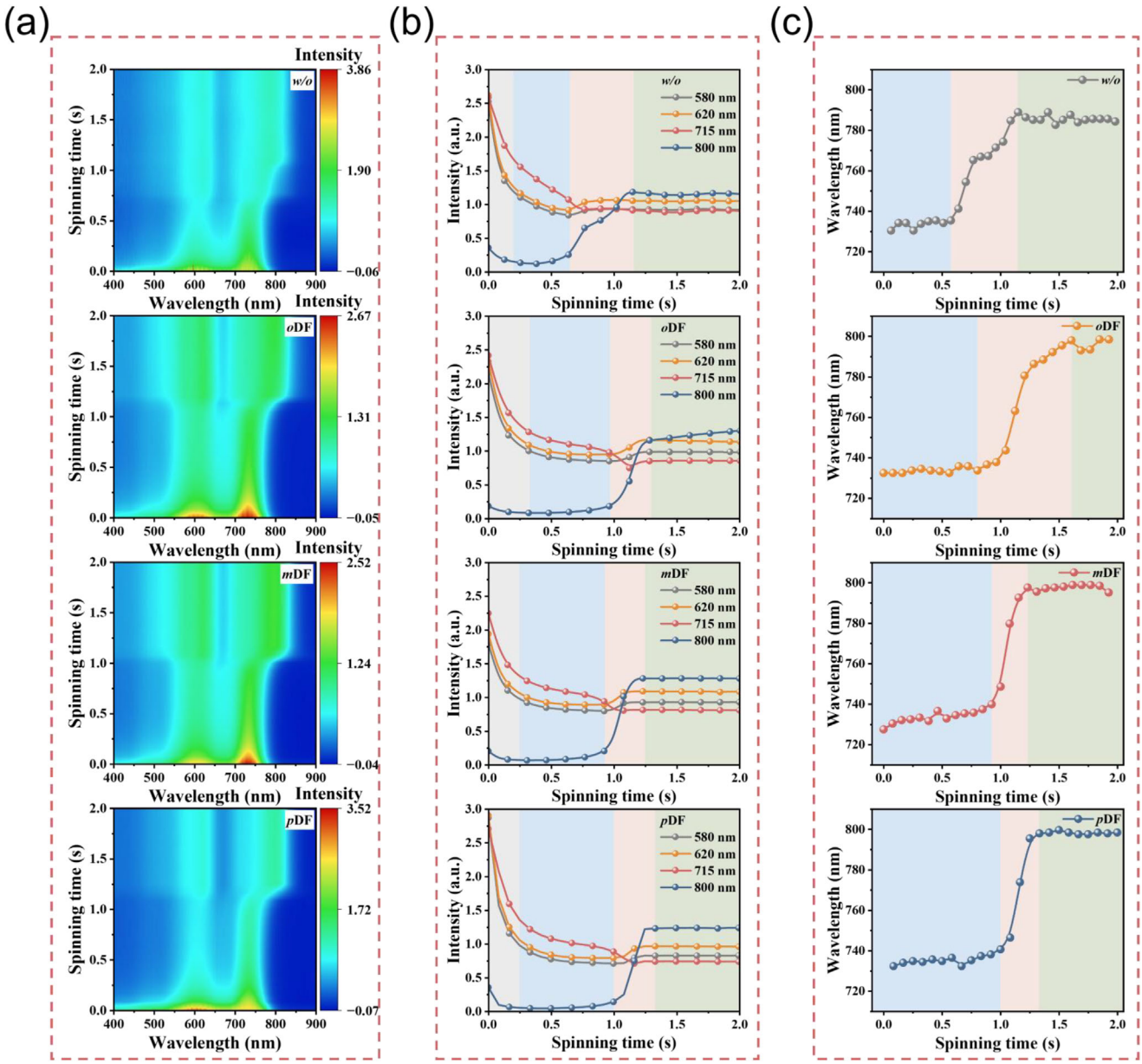

FIGURE 2 | (a) 2D contour maps of in situ UV–vis absorption spectra during spin-coating for PM6:L8-BO blend films treated at different conditions. (b) Time-dependent peak intensity at 580 nm (PM6 0–0), 620 nm (PM6 0–1), 715 nm (L8-BO 0–0), and 800 nm (L8-BO 0–1). (c) L8-BO peak position shifts over time in the in situ spectra.

control. To elucidate the underlying mechanism, we conducted a quantitative analysis of energy loss (E_{loss}), which comprises three components: ΔE_1 and ΔE_2 associated with radiative recombination losses above and below the bandgap, respectively, and ΔE_3, the non-radiative recombination loss ($E_{loss,nr}$). Table 2 and Figure 3h summarize the detailed E_{loss} parameters. As shown in Figure S8, the bandgaps of the as-cast, *o*DF-, *m*DF-, and *p*DF-treated devices are 1.462, 1.462, 1.450, and 1.451 eV, respectively. Notably, ΔE_1 and ΔE_2 remain similar across all samples, indicating that radiative losses do not drive the observed differences. However, ΔE_3 varies significantly: 0.229 eV (*w/o*), 0.294 eV (*o*DF), 0.231 eV (*m*DF), and 0.237 eV (*p*DF), revealing that the higher E_{loss} in the *o*DF-processed device stems from $E_{loss,nr}$. According to the reciprocity principle, ΔE_3 is inversely correlated with the electroluminescence quantum efficiency (EQE_{EL}), following $\Delta E_3 = E_{loss,nr} = -\frac{kT}{q} \ln EQE_{EL}$). A higher EQE_{EL} corresponds to a lower ΔE_3. As shown in Table 2 and Figure 3g, the EQE_{EL} of the *o*DF-based device is significantly reduced by an order of magnitude compared to the control device. In contrast, both the *m*DF- and *p*DF-treated devices maintain EQE_{EL} values comparable to the control, with the quasi-solid *m*DF exhibiting particularly well-preserved luminescence efficiency.

We further validated the effectiveness of *m*DF by incorporating it into D18:L8-BO-based OSC devices. As shown in Figure 3i, a champion device achieves a PCE of 20.08%, along with a V_{OC} of 0.908 V, a J_{SC} of 27.09 mA cm^{-2}, and an FF of 81.63%, demonstrating the exceptional capability for highly efficient OSCs. Additionally, the EQE spectra (Figure S9) demonstrated

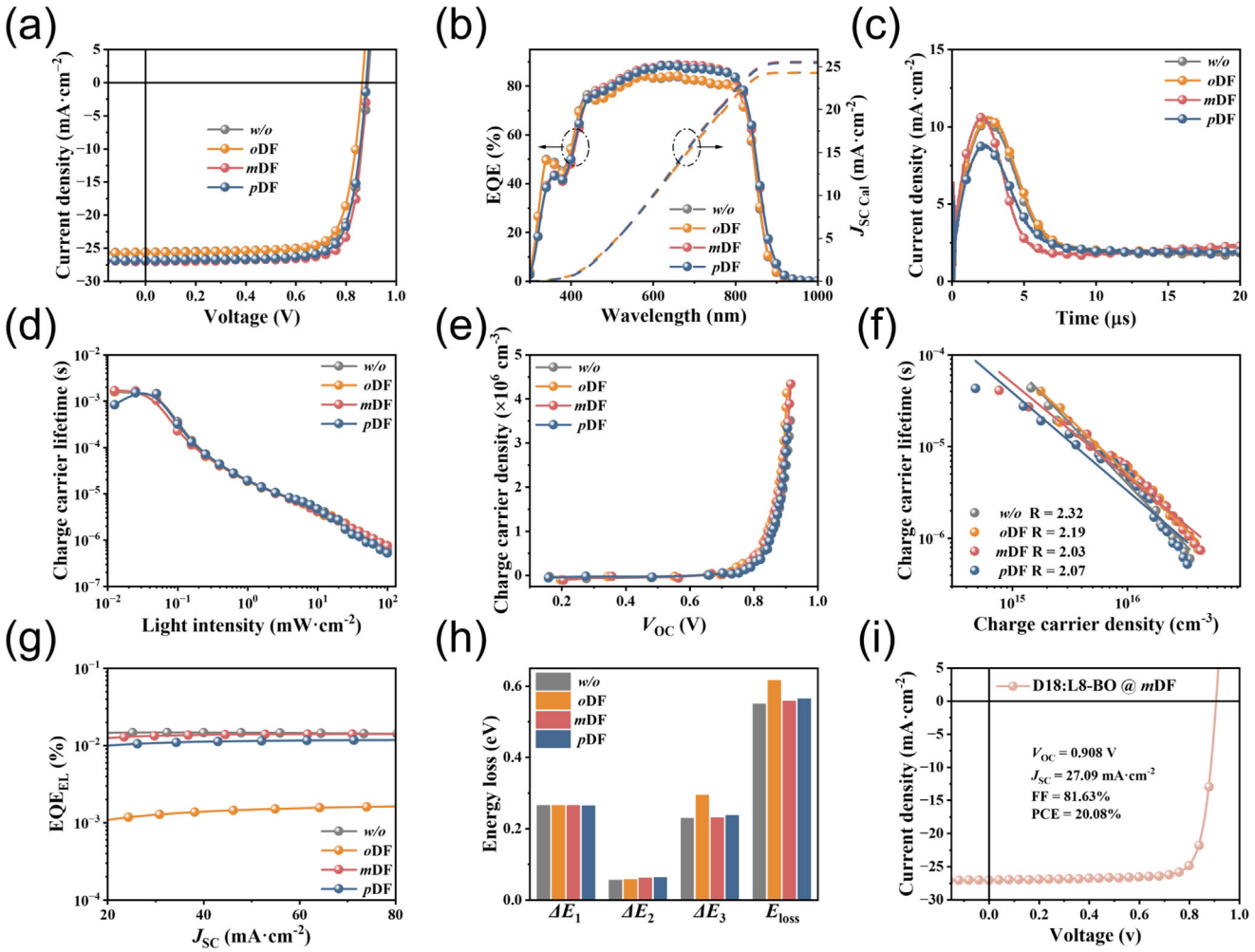

FIGURE 3 | (a) *J*–*V* characteristics of the optimal PM6:L8-BO based OSCs. (b) EQE spectra of the corresponding OSCs. (c) Photo-CELIV curves of the corresponding devices. (d) TPV measurements of the charge carrier lifetime over light intensity. (e) CE measurements of the charge carrier density over V_{OC}. The corresponding lines in (f) are linear fits of the measured data points, with the recombination orders R indicated in the graph. (g) EQE_{EL} plots of the devices under different current density. (h) Detailed E_{loss} values from radiative and non-radiative recombination. (i) *J*–*V* characteristics of the optimal binary OSCs based on *m*DF-treated D18:L8-BO active layer.

TABLE 1 | Detailed device parameters of PM6:L8-BO-based OSCs and average values with standard deviation obtained from 10 devices.

Additive	V_{OC} (V)	J_{SC} (mA cm^{-2})	FF (%)	PCE (%)
w/o	0.889 (0.887±0.001)	25.63 (25.74±0.11)	77.81 (77.03±0.45)	17.72 (17.68±0.08)
*o*DF[a)]	0.867 (0.864±0.002)	25.69 (25.67±0.13)	77.59 (76.92±0.57)	17.28 (17.16±0.15)
*m*DF[a)]	0.885 (0.884±0.001)	27.01 (26.76±0.16)	80.66 (79.90±0.42)	19.28 (18.99±0.16)
*p*DF[a)]	0.883 (0.882±0.001)	26.91 (26.33±0.32)	78.04 (78.54±0.43)	18.54 (18.28±0.17)

[a)]50% of the total mass of PM6 and L8-BO.

TABLE 2 | E_{loss} data of the control, *o*DF, *m*DF, and *p*DF-processed devices.

PM6:L8-BO	E_g (eV)	V_{OC}^{SQ} (eV)	V_{OC}^{rad} (eV)	V_{OC}^{cal} (eV)	ΔE_1 (eV)	ΔE_2 (eV)	ΔE_3 (eV)
w/o	1.462	1.196	1.141	0.912	0.265	0.056	0.229
*o*DF	1.462	1.196	1.139	0.846	0.265	0.057	0.294
*m*DF	1.450	1.185	1.124	0.893	0.265	0.061	0.231
*p*DF	1.451	1.187	1.124	0.887	0.264	0.063	0.237

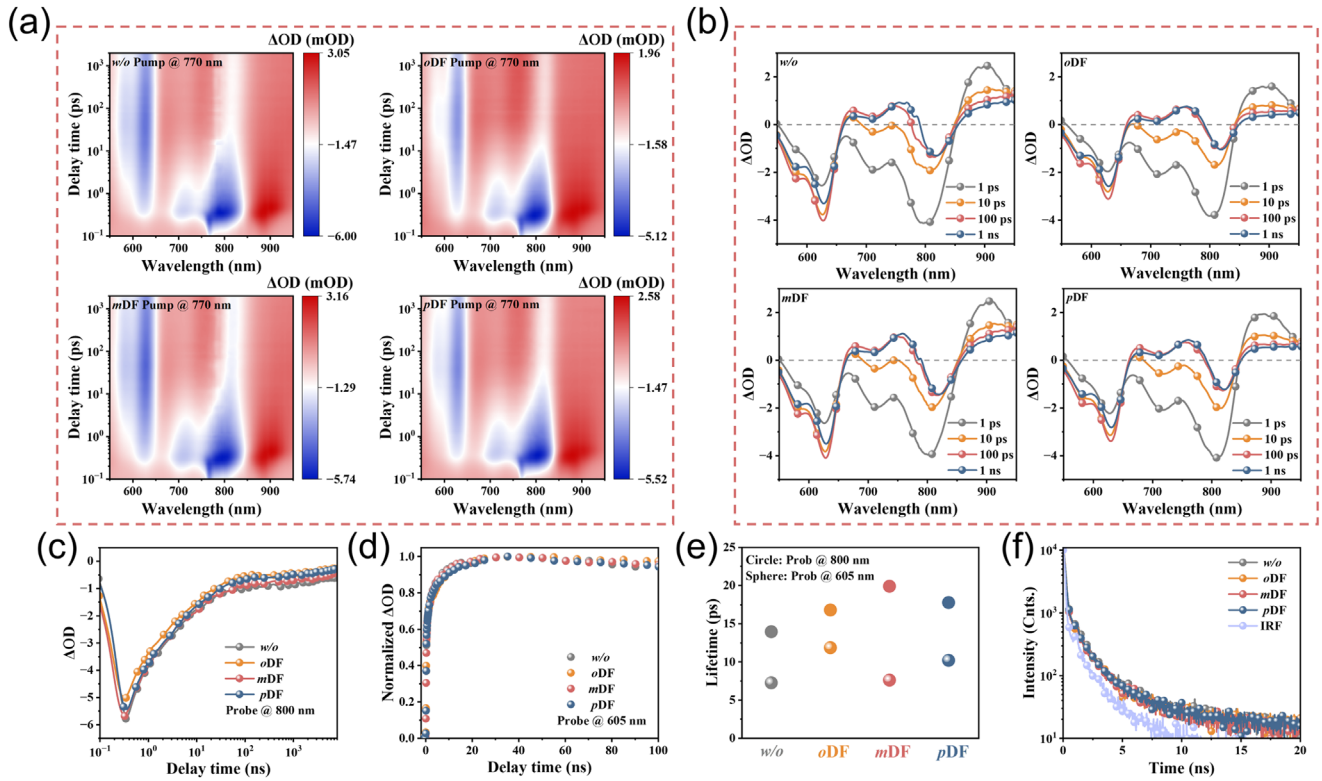

FIGURE 4 | (a) 2D color plot of TAS of PM6:L8-BO blend films. (b) TAS spectra of the films at different time delays. (c) TAS kinetic traces at 800 nm, corresponding to the GSB of L8-BO. (d) TAS kinetic trace at 605 nm, corresponding to the GSB of PM6. (e) TAS kinetic lifetime summary. (f) TRPL of the PM6:L8-BO blend films, excited at 783.3 nm and detected at 837.7 nm.

a broad and efficient photon response spanning 400–900 nm, yielding an integrated J_{SC} of 25.78 mA·cm^{-2}.

Transient absorption spectroscopy (TAS) and time-resolved photoluminescence (TRPL) were employed to probe the photophysical dynamics of the active layer, offering key insights into charge carrier behavior. TAS measurements tracked charge generation, separation, and recombination, with pristine PM6 and L8-BO films excited at 575 and 770 nm, respectively (Figures S10 and S11). Ground state bleach (GSB) signals were observed in the 550–700 nm range for PM6 and 600–875 nm for L8-BO, leading to the selection of 770 nm excitation in blend films to specifically probe hole-generation and transfer. Figure 4a,b presents 2D TAS images and spectra of PM6:L8-BO blends treated at different conditions at various decay times. Upon excitation of the L8-BO, PM6 GSB signals appeared almost instantaneously, indicating ultrafast hole transfer. The decay kinetics at 800 nm (GSB of L8-BO, Figure 4c) and 605 nm (GSB of PM6, Figure 4d) further confirm this process with high temporal resolution. Kinetic analyses reveal the sequential dynamics of exciton generation, dissociation into free carriers (polarons), and subsequent recombination, with detailed parameters summarized in Figure 4e and Table S2. The presence of additives significantly modifies L8-BO exciton behavior, prolonging exciton lifetimes in all treated films, with the most pronounced effect observed for *m*DF. Specifically, the *m*DF-treated blend exhibits the longest exciton lifetime (τ = 19.87 ps), indicating effective suppression of recombination. A comparative analysis of polaron kinetics (Figure 4d) further reveals that hole transfer reaches saturation fastest in the *m*DF-treated film, highlighting its superior charge-transfer efficiency. This enhancement directly correlates with the highest J_{SC} and FF observed in *m*DF-treated devices. Moreover, TRPL measurements and corresponding fits (Table S3) confirm that *m*DF facilitates the most efficient exciton splitting, effectively reducing voltage losses. Collectively, these findings underscore the pivotal role of *m*DF in optimizing charge dynamics and improving PM6:L8-BO device performance.

To further elucidate the impact of additives on device performance, we investigated the microstructure evolution of active layers utilizing atomic force microscopy (AFM) [60]. As illustrated in the height images (Figure 5a), the w/o, *o*DF-, and *p*DF-treated films exhibit similarly smooth surfaces with root-mean-square (RMS) roughness values of 1.13, 1.10, and 1.14 nm, respectively, whereas the *m*DF-treated film shows an increased roughness of 1.24 nm. A rougher surface enhances interfacial contact with the top ETL, potentially facilitating more efficient charge extraction. AFM phase images (Figure S12) further reveal a fibrillar network structure across all blends, with the *m*DF-treated film displaying a more defined fibril texture, characterized by thinner, sparsely distributed fibrils.

GIWAXS analysis probed the crystalline packing of the active layers. The 2D patterns (Figure S13) and corresponding in-plane IP and OOP line profiles (Figure 5b) reveal key structural features, with quantitative parameters summarized in Table S4. Across all blend films, PM6 and L8-BO retain the strong crystalline characteristics of their neat films, exhibiting a dominant face-on orientation. The (100) peaks in the IP direction appear at 0.30 Å^{-1} for all blends, corresponding to an identical d-spacing of 20.95 Å.

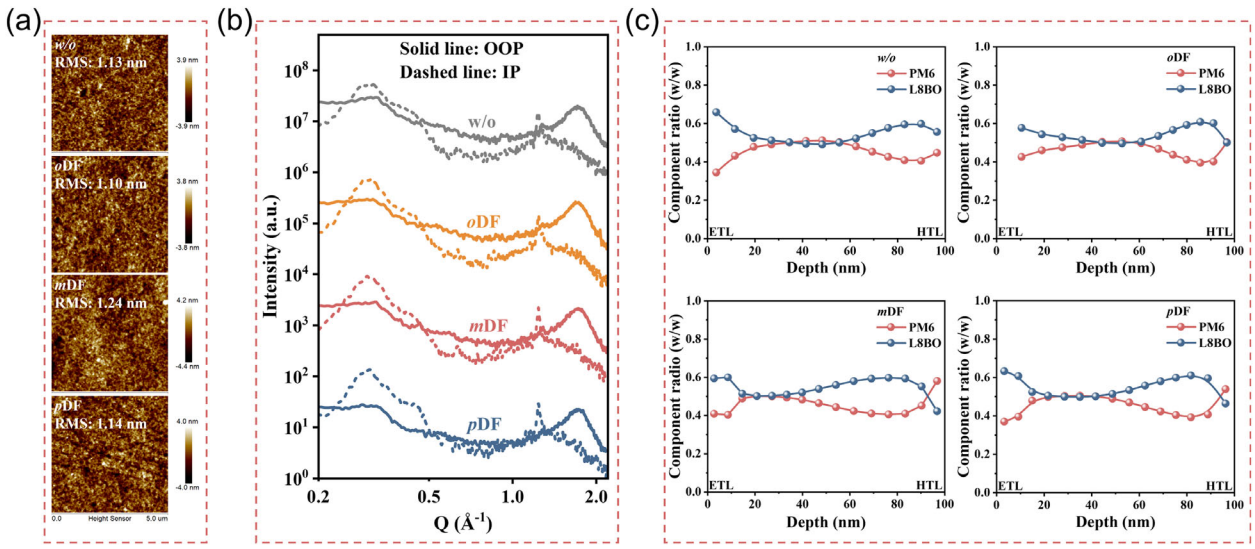

FIGURE 5 | (a) AFM height images, (b) 1D GIWAXS cutline profiles of the optimized blend films. (c) Film-depth composition distribution from depth-dependent absorption spectra.

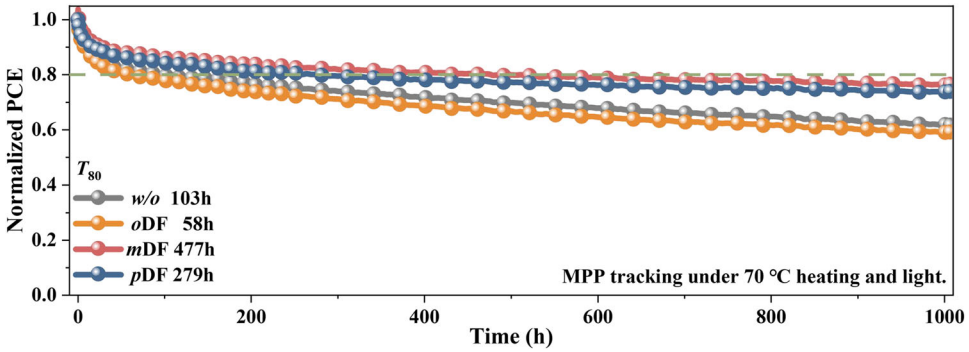

FIGURE 6 | Dynamic MPP tracking for the optimal OSCs under 70°C heating and light.

However, the CLs differ markedly. The *m*DF-treated film exhibits the largest CL (58.44 Å), derived from the narrowest FWHM, indicating the highest degree of crystalline order. The additive-free film shows the shortest CL (41.74 Å), whereas the *o*DF- and *p*DF-treated films display intermediate CLs (both 53.13 Å), reflecting a moderate improvement in crystallinity relative to the control but still below that of the *m*DF sample. In the OOP direction, *m*DF incorporation also optimizes π–π stacking, reducing the stacking distance to 3.59 Å and yielding the longest CL (17.71 Å). By contrast, the additive-free film shows the largest π–π spacing (3.63 Å) and the shortest CL (14.25 Å), while the *o*DF- and *p*DF-treated films give slightly reduced π–π distances (3.61 Å) and increased CLs (16.70 and 17.19 Å), again lying between the control and *m*DF-treated films. These results indicate that the quasi-solid additive *m*DF significantly enhances molecular ordering by reducing π–π stacking distance and increasing crystallite size. Such structural optimizations are key to improving charge transport and overall device performance.

Film-depth-dependent light absorption spectroscopy (FLAS, Figure S14) was employed to further elucidate the impact of various additives on the vertical phase separation morphology of the active layer [61–64]. As shown in Figure 5c, the composition profiles reveal that the addition of quasi-solid *m*DF and solid *p*DF induces a more favorable vertical phase distribution than *o*DF, promoting PM6 enrichment near the bottom of the active layer and L8-BO accumulation toward the top, thereby facilitating more efficient charge extraction and transport. In addition, *m*DF- and *p*DF-treated blends exhibit flatter composition ratio curves, suggesting improved miscibility between PM6 and L8-BO.

Long-term stability is a critical determinant of the practical viability of OSCs. As illustrated in Figure 6, the stability of PM6:L8-BO devices was assessed under dynamic maximum power point (MPP) tracking at 70°C and one-sun equivalent illumination. After 1000 h of continuous tracking, the impact of additives became evident. Compared with additive-free devices (T_{80} = 103 h), those treated with *m*DF and *p*DF exhibited significantly enhanced stability, with T_{80} values of 477 and 279 h, respectively. In contrast, liquid *o*DF-treated devices showed a markedly reduced T_{80} of 58 h. The stability ranking correlates with physical state and the structural metrics above: *m*DF tightens π–π stacking, increases coherence length, and avoids residualadditive penalties, collectively suppressing nonradiative loss pathways and morphological drift during stress.

3 | Conclusion

We systematically elucidate how the physical state of three isomeric, in situ-removable, cold-sublimating additives (*o*DF, *m*DF, and *p*DF) dictates film formation, molecular ordering, and charge transport in PM6:L8-BO binary OSCs. Among them, the quasi-solid *m*DF functions as a cold-sublimating transient structural agent during drying, enhancing molecular packing, shortening the π–π stacking distance, and increasing carrier mobility. Consequently, quasi-solid *m*DF-treated PM6:L8-BO binary OSCs achieve a PCE of 19.28%, surpassing the control (17.72%) and devices treated with *o*DF (17.28%) or *p*DF (18.54%). When applied to D18:L8-BO systems, quasi-solid *m*DF further enables a PCE exceeding 20%. Comprehensive spectroscopy and computational analyses confirm that *m*DF effectively modulates vertical phase separation, prolongs exciton lifetimes, and suppresses recombination losses. Moreover, *m*DF significantly enhances device stability, achieving a T_{80} of 477 h under operational conditions, far outperforming *o*DF (58 h) and *p*DF (279 h). These findings underscore the potential of quasi-solid additives in optimizing OSC morphology and performance. By providing new insights into additive engineering, this study offers valuable strategies for advancing the efficiency and long-term stability of OSCs, paving the way for their commercialization.

Acknowledgements

The authors gratefully acknowledge the financial support of the National Natural Science Foundation of China (52573195, 22179040), the Basic and Applied Basic Research Major Program of Guangdong Province (2019B030302007), and the Guangdong Basic and Applied Basic Research Foundation (2024A1515012693). C.L. gratefully acknowledges the financial support through the Helmholtz Association in the framework of the innovation platform "Solar TAP". C.L. and R. W. are grateful for the financial support from the China Scholarship Council (CSC).

Open access funding enabled and organized by Projekt DEAL.

Conflicts of Interest

The authors declare no conflicts of interest.

Data Availability Statement

The data that support the findings of this study are available from the corresponding author upon reasonable request.

References

1. P. C. Y. Chow and T. Someya, "Organic Photodetectors for Next-Generation Wearable Electronics," *Advanced Materials* 32 (2020): 1902045, https://doi.org/10.1002/adma.201902045.

2. Y. Li, X. Huang, H. K. M. Sheriff, and S. R. Forrest, "Semitransparent Organic Photovoltaics For Building-Integrated Photovoltaic Applications," *Nature Reviews Materials* 8 (2023): 186–201, https://doi.org/10.1038/s41578-022-00514-0.

3. Y. Liu, B. Liu, C.-Q. Ma, et al., "Recent Progress In Organic Solar Cells (Part II Device Engineering)," *Science China Chemistry* 65 (2022): 1457–1497, https://doi.org/10.1007/s11426-022-1256-8.

4. G. Zhang, F. R. Lin, F. Qi, et al., "Renewed Prospects for Organic Photovoltaics," *Chemical Reviews* 122 (2022): 14180–14274, https://doi.org/10.1021/acs.chemrev.1c00955.

5. Z. Zhou, Z. Yuan, Z. Yin, Q. Xue, N. Li, and F. Huang, "Progress Of Semitransparent Emerging Photovoltaics For Building Integrated Applications," *Green Energy & Environment* 9 (2024): 992–1015, https://doi.org/10.1016/j.gee.2023.05.006.

6. L. Wang, C. Chen, Z. Gan, et al., "Diluted Ternary Heterojunctions to Suppress Charge Recombination for Organic Solar Cells With 21% Efficiency," *Advanced Materials* 37 (2025): 2419923, https://doi.org/10.1002/adma.202419923.

7. L. Zhu, M. Zhang, G. Zhou, et al., "Achieving 20.8% Organic Solar Cells Via Additive-Assisted Layer-By-Layer Fabrication With Bulk P-I-N Structure And Improved Optical Management," *Joule* 8 (2024): 3153–3168, https://doi.org/10.1016/j.joule.2024.08.001.

8. R. Ma, Z. Luo, Y. Zhang, et al., "Organic Solar Cells: Beyond 20%," *Science China Materials* 68 (2025): 1689–1701.

9. J. Wu, Y. Li, F. Tang, et al., "Porphyrin-Modified SnO_2 Electron Transport Layer for Efficient and Stable Inverted Organic Solar Cells," *Advanced Functional Materials* 35 (2025): 2504623, https://doi.org/10.1002/adfm.202504623.

10. L. Kong, Z. Zhang, N. Zhao, et al., "In Situ Removable Additive Assisted Organic Solar Cells Achieving Efficiency Over 19% and Fill Factor Exceeding 81%," *Advanced Energy Materials* 13 (2023): 2300763, https://doi.org/10.1002/aenm.202300763.

11. L. Kong, X. Wang, M. Li, et al., "In-Situ Removable Solid Additive Optimizing Active Layer and Cathode Interlayer of Organic Solar Cells," *Advanced Energy Materials* 14 (2024): 2402517, https://doi.org/10.1002/aenm.202402517.

12. Z. Zheng, J. Wang, P. Bi, et al., "Tandem Organic Solar Cell With 20.2% Efficiency," *Joule* 6 (2022): 171–184, https://doi.org/10.1016/j.joule.2021.12.017.

13. H. Tang, Z. Liao, Q. Chen, et al., "Elucidating The Optimal Material Combinations Of Organic Photovoltaics For Maximum Industrial Viability," *Joule* 8 (2024): 2208–2219, https://doi.org/10.1016/j.joule.2024.06.022.

14. H. Tang, Z. Liao, S. Karuthedath, et al., "Rationale For Highly Efficient And Outdoor-Stable Terpolymer Solar Cells," *Energy & Environmental Science* 16 (2023): 2056–2067, https://doi.org/10.1039/D3EE00350G.

15. H. Tang, J. Lv, K. Liu, et al., "Self-Assembly Enables Simple Structure Organic Photovoltaics Via Green-Solvent And Open-Air-Printing: Closing The Lab-To-Fab Gap," *Materials Today* 55 (2022): 46–55, https://doi.org/10.1016/j.mattod.2022.04.005.

16. J. Wu, F. Tang, S. Wu, et al., "Interface Modification of Tin Oxide Electron-Transport Layer for the Efficiency and Stability Enhancement of Organic Solar Cells," *Advanced Energy Materials* 14 (2024): 2302932, https://doi.org/10.1002/aenm.202302932.

17. G. Yu, J. Gao, J. C. Hummelen, F. Wudl, and A. J. Heeger, "Polymer Photovoltaic Cells: Enhanced Efficiencies via a Network of Internal Donor-Acceptor Heterojunctions," *Science* 270 (1995): 1789–1791, https://doi.org/10.1126/science.270.5243.1789.

18. F. Zhao, C. Wang, and X. Zhan, "Morphology Control in Organic Solar Cells," *Advanced Energy Materials* 8 (2018): 1703147, https://doi.org/10.1002/aenm.201703147.

19. M. Ghasemi, N. Balar, Z. Peng, et al., "A Molecular Interaction–Diffusion Framework For Predicting Organic Solar Cell Stability," *Nature Materials* 20 (2021): 525–532, https://doi.org/10.1038/s41563-020-00872-6.

20. C. Cui and Y. Li, "Morphology Optimization Of Photoactive Layers In Organic Solar Cells," *Aggregate* 2 (2021): 31.

21. S. Siddika, Z. Peng, N. Balar, et al., "Molecular Interactions That Drive Morphological And Mechanical Stabilities In Organic Solar Cells," *Joule* 7 (2023): 1593–1608, https://doi.org/10.1016/j.joule.2023.06.002.

22. H. Tang, C. Yan, J. Huang, et al., "Benzodithiophene-Based Small-Molecule Donors for Next-Generation All-Small-Molecule Organic Photovoltaics," *Matter* 3 (2020): 1403–1432, https://doi.org/10.1016/j.matt.2020.09.001.

23. J. Yu, S. Li, M. Shi, H. Zhu, and H. Chen, "Recent Advances in Thermo- and Photostabilities of Organic Solar Cells: Material Design and Morphology Control," *Polymer Science & Technology* 1 (2025): 25–45, https://doi.org/10.1021/polymscitech.4c00054.

24. C. Li, X. Gu, Z. Chen, et al., "Achieving Record-Efficiency Organic Solar Cells upon Tuning the Conformation of Solid Additives," *Journal of the American Chemical Society* 144 (2022): 14731–14739, https://doi.org/10.1021/jacs.2c05303.

25. Y. Yan, B. Duan, M. Ru, Q. Gu, S. Li, and W. Zhao, "Toward Flexible and Stretchable Organic Solar Cells: A Comprehensive Review of Transparent Conductive Electrodes, Photoactive Materials, and Device Performance," *Advanced Energy Materials* 15: 2404233, https://doi.org/10.1002/aenm.202404233.

26. C.-L. Tsai, K.-E. Hung, H.-C. Lu, C.-C. Tseng, F.-Y. Cao, and Y.-J. Cheng, "Volatile and non-volatile additives for Polymer Solar cells From Fullerene to non-fullerene systems," *Journal of Polymer Research* 30 (2023): 404, https://doi.org/10.1007/s10965-023-03784-6.

27. Y. Zhang, H. Xia, J. Yu, Y. Yang, and G. Li, "Materials and Device Engineering Perspective: Recent Advances in Organic Photovoltaics," *Advanced Materials* (2025): 2504063, https://doi.org/10.1002/adma.202504063.

28. W. Zhang, K. Zhang, and X. Hao, "Multilength-Scale Morphological Engineering for Stable Organic Solar Cells," *Small* 21 (2025): 2412230, https://doi.org/10.1002/smll.202412230.

29. H. Liu, D. Yuan, H. Jiang, S. Li, L. Zhang, and J. Chen, "Siloxane-Induced Robust Photoactive Materials With High Humidity Tolerance For Ambient Processing Of Organic Solar Cells," *Energy & Environmental Science* 16 (2023): 3474–3485, https://doi.org/10.1039/D3EE01393F.

30. H. Liu, X. Xie, L. Zhang, J. Wang, and J. Chen, "Siloxane as Humidity-Resistant and Stabilizing Additive for Ambient-Processed Organic Solar Cells," *Advanced Energy Materials* 15 (2025): 2404679, https://doi.org/10.1002/aenm.202404679.

31. H. Liu, Z. Zhang, D. Yuan, et al., "Orthogonal solvent-sequential deposition of a nonfullerene acceptor solution on polymer donor film: Complete interpenetration and highly efficient inverted organic solar cells," *Journal of Materials Chemistry A* 11 (2023): 19860–19869.

32. J. K. Lee, W. L. Ma, C. J. Brabec, et al., "Processing Additives for Improved Efficiency From Bulk Heterojunction Solar Cells," *Journal of the American Chemical Society* 130 (2008): 3619–3623, https://doi.org/10.1021/ja710079w.

33. C. V. Hoven, X.-D. Dang, R. C. Coffin, J. Peet, T.-Q. Nguyen, and G. C. Bazan, "Improved Performance of Polymer Bulk Heterojunction Solar Cells Through the Reduction of Phase Separation via Solvent Additives," *Advanced Materials* 22 (2010): E63–E66, https://doi.org/10.1002/adma.200903677.

34. S. Kwon, H. Kang, J.-H. Lee, et al., "Effect of Processing Additives on Organic Photovoltaics: Recent Progress and Future Prospects," *Advanced Energy Materials* 7 (2017): 1601496, https://doi.org/10.1002/aenm.201601496.

35. B. J. Tremolet de Villers, K. A. O'Hara, D. P. Ostrowski, et al., "Removal of Residual Diiodooctane Improves Photostability of High-Performance Organic Solar Cell Polymers," *Chemistry of Materials* 28 (2016): 876–884, https://doi.org/10.1021/acs.chemmater.5b04346.

36. Y.-F. Ma, Y. Zhang, and H.-L. Zhang, "Solid additives in organic solar cells: Progress and perspectives," *Journal of Materials Chemistry C* 10 (2022): 2364–2374, https://doi.org/10.1039/D1TC04224F.

37. D. Hu, H. Tang, C. Chen, et al., "Solid Additive Engineering for Next-generation Organic Photovoltaics," *Advanced Materials* 36 (2024): 2406949, https://doi.org/10.1002/adma.202406949.

38. J. Fu, H. Chen, P. Huang, et al., "Eutectic Phase Behavior Induced By A Simple Additive Contributes To Efficient Organic Solar Cells," *Nano Energy* 84 (2021): 105862.

39. L. Zhu, M. Zhang, J. Xu, et al., "Single-Junction Organic Solar Cells With Over 19% Efficiency Enabled By A Refined Double-Fibril Network Morphology," *Nature Materials* 21 (2022): 656–663, https://doi.org/10.1038/s41563-022-01244-y.

40. C. Li, J. Zhou, J. Song, et al., "Non-Fullerene Acceptors With Branched Side Chains And Improved Molecular Packing To Exceed 18% Efficiency In Organic Solar Cells," *Nature Energy* 6 (2021): 605–613, https://doi.org/10.1038/s41560-021-00820-x.

41. S. Bao, H. Yang, H. Fan, et al., "Volatilizable Solid Additive-Assisted Treatment Enables Organic Solar Cells With Efficiency Over 18.8% and Fill Factor Exceeding 80%," *Advanced Materials* 33 (2021): 2105301, https://doi.org/10.1002/adma.202105301.

42. B. Fan, W. Zhong, W. Gao, et al., "Understanding the Role of Removable Solid Additives: Selective Interaction Contributes to Vertical Component Distributions," *Advanced Materials* 35 (2023): 2302861, https://doi.org/10.1002/adma.202302861.

43. C. Zhang, T. Heumueller, S. Leon, et al., "A Top-Down Strategy Identifying Molecular Phase Stabilizers To Overcome Microstructure Instabilities In Organic Solar Cells," *Energy & Environmental Science* 12 (2019): 1078–1087, https://doi.org/10.1039/C8EE03780A.

44. S. Chen, J. Ye, Q. Yang, et al., "Molecular Ordering And Phase Segregation Induced By A Volatile Solid Additive For Highly Efficient All-Small-Molecule Organic Solar Cells," *Journal of Materials Chemistry A* 9 (2021): 2857–2863, https://doi.org/10.1039/D0TA10649F.

45. X. Song, H. Xu, X. Jiang, et al., "Film-Formation Dynamics Coordinated By Intermediate State Engineering Enables Efficient Thickness-Insensitive Organic Solar Cells," *Energy & Environmental Science* 16 (2023): 3441–3452, https://doi.org/10.1039/D3EE01320K.

46. M. Wang, T. Chen, Y. Li, et al., "Synergistically optimizing the optoelectronic properties and morphology using a photo-active solid additive for high-performance binary organic photovoltaics," *Energy & Environmental Science* 17 (2024): 2598–2609, https://doi.org/10.1039/D3EE04065H.

47. D. Zhang, Y. Li, M. Li, et al., "Targeted Adjusting Molecular Arrangement in Organic Solar Cells via a Universal Solid Additive," *Advanced Functional Materials* 32 (2022): 2205338, https://doi.org/10.1002/adfm.202205338.

48. R. Yu, H. Yao, Z. Chen, et al., "Enhanced π–π Interactions of Nonfullerene Acceptors by Volatilizable Solid Additives in Efficient Polymer Solar Cells," *Advanced Materials* 31 (2019): 1900477, https://doi.org/10.1002/adma.201900477.

49. D. Li, S. Liang, X. Hua, et al., "Selecting Solid Additives to Control the Interaction Between Polymer Donors and Additives for Constructing High-Efficiency Organic Solar Cells," *Macromolecules* 57 (2024): 3580–3587, https://doi.org/10.1021/acs.macromol.4c00362.

50. Q. Liang, W. Li, H. Lu, et al., "Recent Advances of Solid Additives Used in Organic Solar Cells: Toward Efficient and Stable Solar Cells," *ACS Applied Energy Materials* 6 (2023): 31–50, https://doi.org/10.1021/acsaem.2c03180.

51. W. A. Memon, Z. Deng, and F. He, "Recent Development In Solid Additives Enables High-Performance Organic Solar Cells," *EnergyChem* 6 (2024): 100129, https://doi.org/10.1016/j.enchem.2024.100129.

52. J. Song, L. Ye, C. Liu, et al., "Multifunctional Solid Additive Enables All-Polymer Solar Cells With Improved Efficiency, Photostability And Mechanical Durability," *Energy & Environmental Science* 16 (2023): 5371–5380, https://doi.org/10.1039/D3EE02953K.

53. Y. Xie, H. S. Ryu, L. Han, et al., "High-Efficiency Organic Solar Cells Enabled By An Alcohol-Washable Solid Additive," *Science China Chemistry* 64 (2021): 2161–2168, https://doi.org/10.1007/s11426-021-1121-y.

54. S. T. Turner, P. Pingel, R. Steyrleuthner, E. J. W. Crossland, S. Ludwigs, and D. Neher, "Quantitative Analysis of Bulk Heterojunction Films Using Linear Absorption Spectroscopy and Solar Cell Performance," *Advanced*

Functional Materials 21 (2011): 4640–4652, https://doi.org/10.1002/adfm.201101583.

55. M. S. Vezie, S. Few, I. Meager, et al., "Exploring The Origin Of High Optical Absorption In Conjugated Polymers," *Nature Materials* 15 (2016): 746–753, https://doi.org/10.1038/nmat4645.

56. R. Wang, L. Han, N. Li, et al., "Reducing Voltage Losses in Organic Photovoltaics Requires Interfacial Disorder Management," *Advanced Energy Materials* 14 (2024): 2400609, https://doi.org/10.1002/aenm.202400609.

57. C. Liu, L. Lüer, V. M. L. Corre, et al., "Understanding Causalities In Organic Photovoltaics Device Degradation In A Machine-Learning-Driven High-Throughput Platform," *Advanced Materials* 36 (2024): 2300259, https://doi.org/10.1002/adma.202300259.

58. X. Du, L. Lüer, T. Heumueller, et al., "Elucidating the Full Potential of OPV Materials Utilizing a High-Throughput Robot-Based Platform and Machine Learning," *Joule* 5 (2021): 495–506, https://doi.org/10.1016/j.joule.2020.12.013.

59. R. Wang, L. Lüer, S. Langner, et al., "Understanding the Microstructure Formation of Polymer Films by Spontaneous Solution Spreading Coating With a High-Throughput Engineering Platform," *Chemsuschem* 14 (2021): 3590–3598, https://doi.org/10.1002/cssc.202100927.

60. N. Wei, H. Lu, Y. Wei, et al., "Constructing A Dual-Fiber Network In High Efficiency Organic Solar Cells Via Additive-Induced Supramolecular Interactions With Both Donor And Acceptor," *Energy & Environmental Science* 18 (2025): 2298–2307, https://doi.org/10.1039/D4EE05375C.

61. G. Lu, Z. Shen, H. Wang, L. Bu, and G. Lu, "Optical Interference On The Measurement Of Film-Depth-Dependent Light Absorption Spectroscopy And A Correction Approach," *Review of Scientific Instruments* 94 (2023): 023907, https://doi.org/10.1063/5.0138336.

62. L. Bu, M. Hu, W. Lu, Z. Wang, and G. Lu, "Printing Semiconductor–Insulator Polymer Bilayers for High-Performance Coplanar Field-Effect Transistors," *Advanced Materials* 30 (2018): 1704695, https://doi.org/10.1002/adma.201704695.

63. J. Yu, Z. Shen, W. Lu, et al., "Composition Waves in Solution-Processed Organic Films and Its Propagations From Kinetically Frozen Surface Mesophases," *Advanced Functional Materials* 33 (2023): 2302089, https://doi.org/10.1002/adfm.202302089.

64. Z. Shen, J. Yu, G. Lu, et al., "Surface Crystallinity Enhancement In Organic Solar Cells Induced By Spinodal Demixing Of Acceptors And Additives," *Energy & Environmental Science* 16 (2023): 2945–2956, https://doi.org/10.1039/D3EE00090G.

Supporting Information

Additional supporting information can be found online in the Supporting Information section.

Supporting File: aenm70493-sup-0001-SuppMat.docx